$4f^{n-1}5d \to 4f^n$ emission of Ce^{3+}, Pr^{3+}, Nd^{3+}, Er^{3+}, and Tm^{3+} in $LiYF_4$ and YPO_4

P. S. Peijzel,* P. Vergeer, and A. Meijerink

Debye Institute, Utrecht University, P.O. Box 80 000, 3508 TA Utrecht, The Netherlands

M. F. Reid

Department of Physics and Astronomy, University of Canterbury, Christchurch, New Zealand

L. A. Boatner

Condensed Matter Sciences Division, Oak Ridge National Laboratory, Oak Ridge, Tennessee 37831, USA

G. W. Burdick

Department of Physics, Andrews University, Berrien Springs, Michigan 49104, USA

High-resolution $4f^{n-1}5d \to 4f^n$ emission spectra in the (vacuum) ultraviolet are reported for Ce^{3+}, Pr^{3+}, Nd^{3+}, Er^{3+}, and Tm^{3+} in $LiYF_4$ and YPO_4 host lattices. The positions and intensities of the zero-phonon lines are calculated and compared to the high-resolution emission spectra. For the thulium samples gated detection has been used to distinguish between the spin-forbidden and spin-allowed $4f^{n-1}5d \to 4f^n$ emissions. Luminescence lifetimes for the spin-forbidden $4f^{n-1}5d \to 4f^n$ emissions are calculated and compared with experimentally observed lifetimes. A good agreement between experiment and theory is found, demonstrating the validity of the model developed for the $4f^{n-1}5d$ and $4f^n$ states of lanthanide ions.

I. INTRODUCTION

More than a century of spectroscopy of lanthanide ions has involved detailed studies of the intraconfigurational $4f^n \leftrightarrow 4f^n$ transitions. Most of the aspects of these transitions are currently understood quite well. Models have been developed for the energy-level structure and transition probabilities, and with the rapid increase of computer power, it is presently possible to explain and predict the optical spectra of lanthanide ions. An illustrative example is reported in Ref. 1 where the possibility for emission from the $^3P_2$ level of holmium was predicted on the basis of calculations before it was observed.

For interconfigurational $4f^n \leftrightarrow 4f^{n-1}5d$ transitions the situation is different. One of the reasons for this is the fact that these transitions are mainly situated in the ultraviolet and vacuum ultraviolet region, and were studied thoroughly only during the last two decades, triggered by an increased interest in the high-energy excited states of lanthanide ions. The possible application of lanthanide ions in new phosphors combined with the availability of high-intensity sources of VUV radiation like the synchrotron has greatly contributed to the knowledge of the $4f^{n-1}5d$ levels of all lanthanide ions in a number of host lattices.

Recently van Pieterson *et al.* have shown that it is possible to calculate the energies of $4f^n \leftrightarrow 4f^{n-1}5d$ transitions using an extension of the model used for $4f^n$ levels by including crystal field and spin-orbit interactions for the $5d$ electron and the Coulomb interaction between the $4f$ and $5d$ electrons.[2,3] The model developed by van Pieterson *et al.* for the energies of $4f^{n-1}5d$ states relies mainly on high-resolution $4f^n \to 4f^{n-1}5d$ excitation spectra for experimental verification. Emission spectra could only be recorded with a poor spectral resolution. Recently, Chen *et al.*[4] reported

a high-resolution $4f^{n-1}5d \to 4f^{11}$ emission band for $LiYF_4:Er^{3+}$.

In the present work we report high-resolution $4f^{n-1}5d \to 4f^n$ emission spectra for various lanthanide ions in $LiYF_4$ and YPO_4. This allows a more detailed study of the positions and intensities of the zero-phonon lines, together with the fine structure caused by vibronic transitions in the emission spectra. $4f^{n-1}5d \to 4f^n$ emission is expected for Ce^{3+}, Pr^{3+}, Nd^{3+}, Er^{3+}, and Tm^{3+} in $LiYF_4$ and YPO_4, except for $YPO_4:Tm^{3+}$ where the charge transfer band is situated below the $4f^{11}5d$ band. The other lanthanide ions do not show $4f^{n-1}5d \to 4f^n$ emission due to the presence of $4f^n$ levels just below the lowest $4f^{n-1}5d$ state, allowing fast nonradiative decay to the $4f^n$ levels. This work will focus on the $4f^{n-1}5d \to 4f^n$ emission spectra of Ce^{3+}, Pr^{3+}, Nd^{3+}, Er^{3+}, and Tm^{3+} in $LiYF_4$ and YPO_4. High-resolution emission spectra are reported and compared with the calculated spectra.

II. THEORY

The $4f^{n-1}5d$ energy levels can be calculated by using an extended version of the model for the $4f^n$ configurations.[2,3,5] The $4f^n$ energy levels are calculated using a parametrized Hamiltonian that contains parameters for the electron interactions and crystal-field parameters which describe the interaction of the ion and its ligands.

In short, the Hamiltonian is written as

$$\mathcal{H}(ff) = \mathcal{H}_A(ff) + \mathcal{H}_{CF}(ff), \tag{1}$$

where the atomic part $\mathcal{H}_A(ff)$ contains electronic interactions (Coulomb and spin-orbit). The crystal field interactions are represented by $\mathcal{H}_{CF}(ff)$.

The full expression for $\mathcal{H}_A(ff)$ is

$$\mathcal{H}_A(ff) = \sum_k F^k(ff)f_k(ff) + \zeta(ff)A_{SO}(ff) + \alpha(ff)L(L+1)$$

$$+ \beta(ff)G(G_2) + \gamma(ff)G(R_7) + \sum_i T^i(ff)t_i(ff)$$

$$+ \sum_k P^k(ff)p_k(ff) + \sum_j M^j(ff)m_j(ff), \qquad (2)$$

with $k=2,4,6$, $i=2,3,4,6,7,8$, and $j=0,2,4$. The Coulomb interaction is parametrized by the F^k parameters. $\zeta(ff)$ defines the spin-orbit interaction. The two- and three-body correlations are parametrized by $\alpha(ff)$, $\beta(ff)$, $\gamma(ff)$, and $T^i(ff)$. Higher-order magnetic interactions are parametrized by $M^j(ff)$ and $P^k(ff)$.

The crystal-field splitting of the $4f^n$ states is determined by

$$\mathcal{H}_{CF}(ff) = \sum_{k,q} B_q^k(ff)C_q^{(k)}(ff), \qquad (3)$$

where the $B_q^k(ff)$ parameters define the radially dependent part of the one-electron crystal-field interaction and $C_q^{(k)}(ff)$ are the many-electron spherical tensor operators for the $4f^n$ configuration. For configurations concerning $4f$ electrons the values of k are restricted to 2, 4, and 6. The applicable values of q depend on the site symmetry of the lanthanide ion in the host lattice. Rare-earth ions in LiYF$_4$ occupy sites with S_4 symmetry with only a small deviation from D_{2d} symmetry. D_{2d} is the exact site symmetry for rare-earth ions in YPO$_4$. For D_{2d} symmetry[6] the allowed values for q are 0 and ±4.

To expand the well-known model for the calculation of $4f^n$ energy levels to $4f^{n-1}5d$ configurations extra contributions involving the d electron have to be included.[2] These are the spin-orbit interaction for the d electron, the crystal-field interactions of the d electron, and the Coulomb interaction between the $4f$ electron and the $5d$ electron. The addition to the Hamiltonian is

$$\mathcal{H}(fd) = \mathcal{H}_A(fd) + \mathcal{H}_A(dd) + \mathcal{H}_{CF}(dd). \qquad (4)$$

The atomic Hamiltonian is written as

$$\mathcal{H}_A(fd) = \Delta_E(fd) + \sum_k F^k(fd)f_k(fd) + \sum_j G^j(fd)g_j(fd), \qquad (5)$$

$$\mathcal{H}_A(dd) = \zeta_{SO}(dd)A_{SO}(dd), \qquad (6)$$

with $k=2$ and 4, $j=1,3,5$. $F^k(fd)$ and $G^j(fd)$ are the direct and exchange Slater parameters, respectively, for the Coulomb interaction between the d electron and the $4f$ electrons. $\zeta_{SO}(dd)$ represents the spin-orbit interaction for the $5d$ electron.

The $5d$ levels are also split by the crystal field. This is parametrized by $\mathcal{H}_{CF}(dd)$:

$$\mathcal{H}_{CF}(dd) = \sum_{k,q} B_q^k(dd)C_q^{(k)}(dd), \qquad (7)$$

where k is limited to 2 and 4, while q can be 0 or ±4 for D_{2d} symmetry.

The term $\Delta_E(fd)$ defines the energy difference between the $4f^n$ ground state and the barycenter of the $4f^{n-1}5d$ excited state. Adjusting this value does not influence the splitting of the $5d$ levels, it shifts them all by the same energy.

Emissions from the $4f^{n-1}5d$ excited state to the $4f^n$ ground states are allowed electric dipole transitions, and it is possible to calculate the matrix elements of the electric dipole operator for these transitions. Electrons in $5d$ orbitals do participate in the chemical bond between the lanthanide ion and its ligands. As a result, $4f^n \leftrightarrow 4f^{n-1}5d$ transitions are characterized by a much stronger electron-phonon coupling than $4f^n \leftrightarrow 4f^n$ transitions. Typical Huang-Rhys factors for $4f^n \leftrightarrow 4f^{n-1}5d$ transitions range from 1.5 to 5. This causes most of the intensity to show up in the vibronic bands of the emission spectra. In our model, a Gaussian shape of the vibronic band is assumed, due to the superposition of coupling with several vibrational modes. The energy-level calculations provide the positions of the zero-phonon lines of the emissions, and Gaussian-shaped bands are superimposed on those lines. The energy difference between the zero-phonon line and the maximum of the Gaussian band can be estimated[2] from the $4f \rightarrow 5d$ band in the excitation spectrum of Ce^{3+}.

The radiative transition probability from the initial state $\nu\Gamma_{fd}$ to the final state $\nu'\Gamma_f$ is given by[7]

$$A(\text{ED}) = \frac{1}{4\pi\epsilon_0}\frac{4n\omega^3}{3\hbar c^3}\left(\frac{E_{loc}}{E}\right)^2\frac{1}{g_{fd}}S_{tot}(\nu\Gamma_{fd}\nu'\Gamma_f). \qquad (8)$$

In this equation ϵ_0 is the vacuum permittivity, n is the refractive index, ω is the angular frequency of the emission, $(E_{loc}/E)^2$ is the local field correction, and g_{fd} is the degeneracy of the excited state. We used a refractive index of 1.46 for LiYF$_4$ and 1.75 for YPO$_4$ which is a good approximation for the average value of n in the wavelength region of the emissions studied.[8] The local field correction[9] is given by $[(n^2+2)/3]^2$. The total electric dipole strength S_{tot} is the sum of its components

$$S_{tot} = S_x + S_y + S_z, \qquad (9)$$

where

$$S_{x,y} = \sum_{\gamma_f,\gamma_{fd}} \frac{1}{2}|\langle\nu'\Gamma_f\gamma_f|erC_{-1}^1|\nu\Gamma_{fd}\gamma_{fd}\rangle$$

$$\pm \langle\nu'\Gamma_f\gamma_f|erC_1^1|\nu\Gamma_{fd}\gamma_{fd}\rangle|^2, \qquad (10)$$

$$S_z = \sum_{\gamma_f,\gamma_{fd}} |\langle\nu'\Gamma_f\gamma_f|erC_0^1|\nu\Gamma_{fd}\gamma_{fd}\rangle|^2. \qquad (11)$$

The summation in Eqs. (10) and (11) is over the squared transition dipole moments from the excited states $\nu\Gamma_{fd}$ to the final states $\nu'\Gamma_f$. C_q^1 is a spherical tensor operator as defined in Refs. 10 and 11. The lifetime of the emissions was calculated by taking the inverse of the spontaneous transition probability $A(\text{ED})$. Radial integrals $\langle 5d|r|4f\rangle$ were calculated using Cowan's program.[10]

III. EXPERIMENT

Microcrystalline powders of YPO$_4$ doped with 1% R^{3+} ($R=$Ce,Pr,Nd,Er,Tm) were prepared by firing a mixture of

Y_2O_3 (99.99%), the corresponding R_2O_3 (99.99%), and $(NH_4)_2HPO_4$ in air at 1350 °C for 3 h. A YPO_4 crystal doped with 2% of Nd^{3+} was grown at the Oak Ridge National Laboratory as described in Ref. 12. A microcrystalline powder of $LiYF_4$ doped with 0.1% Pr^{3+} was prepared by firing a mixture of YF_3, LiF, and PrF_3 in stoichiometric ratios (with a 10% excess of LiF) in a flow of ultrapure nitrogen at 600 °C.

$LiYF_4$ single crystals containing 1% –4% of R ions were grown using a Philips PH 1006/13 high-frequency furnace with LiF, YF_3, and RF_3 as the starting compounds. The crystal growth melt contained a 15% excess of LiF. The reactants were mixed and transferred to a vitreous carbon crucible. In order to remove water and oxygen the sample was heated overnight at 300 °C in a flow of ultrapure nitrogen. Subsequently the temperature was raised to 550 °C and SF_6 was introduced in the reaction chamber for 30 min to remove the last traces of water and oxygen. During the rest of the synthesis a nitrogen atmosphere was maintained. The sample was heated until melting was observed. Next, the sample was cooled to room temperature in 10 h.

Both the $LiYF_4$ and YPO_4 samples were checked for phase purity by recording a powder diffractogram using a Philips PW1729 x-ray diffractometer using $CuK\alpha$ radiation. All samples were single phase.

Emission measurements were performed at liquid helium temperatures using a cold-finger type Oxford Instruments liquid helium flow cryostat, equipped with MgF_2 windows. The excitation source consisted of a TuiLaser ExciStar S-200 F_2 laser producing 1-mJ pulses of approximately 10 ns at 157 nm using fluorine and 10-mJ pulses at 193 nm using an argon/fluorine mixture, both with a repetition rate of 100 Hz. Emission spectra were recorded using a 0.55 m Jobin Yvon TRIAX 550 monochromator with a 3600 lines/mm grating blazed for the VUV. The emission was detected using a Hamamatsu R166UHP or R7154 solar blind photomultiplier tube for the VUV and UV emissions up to 300 nm. The spectral response of the system in the UV and VUV is not known which makes it impossible to correct the measured emission spectra for the spectral response. However, based on the typical response curves for the grating and photomultiplier, we expect a flat response between 170 and 250 nm and a strong decrease in sensitivity below 165 nm. Emission between 300 and 700 nm was detected using a Hamamatsu R928 photomultiplier tube, in combination with a 1200-lines/mm grating blazed at 400 nm. For the emission spectra of thulium-doped samples, gated detection was performed using a Stanford Research SR400 boxcar averager. Luminescence lifetime measurements were performed using a Tectronix 2440 digital oscilloscope.

IV. RESULTS AND DISCUSSION

A. Parameter values

The zero-phonon lines in the $4f^{n-1}5d \to 4f^n$ emission spectra originate from transitions from the lowest $4f^{n-1}5d$ state to the different crystal-field levels of the $4f^n$ final levels. For every zero-phonon line a vibronic sideband with fine

structure is present. In order to have a better agreement between the measured and calculated splitting of the $4f^n$ multiplets, we refitted the parameter values for the calculation of the $4f^n$ levels to the experimental values for the energy levels reported for Pr^{3+} (Ref. 13 and 14), Nd^{3+} (Ref. 14 and 15), Er^{3+} (Ref. 16 and 17), and Tm^{3+} (Ref. 18) in $LiYF_4$ and YPO_4. Due to the continuous improvements in the model and computer programs for the energy-level calculations, it is possible to obtain a significantly better agreement between the calculated and observed energy levels than with the parameter values reported previously.[13–18] Since the positions of the zero-phonon lines depend strongly on the positions of the $4f^n$ final states, the use of better parameter values gives a better agreement between the calculated and experimentally observed $4f^{n-1}5d \to 4f^n$ emission spectra. The improved values for the fitting parameters are summarized in Table I. Parameters that were kept fixed in the fitting procedure are indicated in brackets. For Pr^{3+} and Nd^{3+} in $LiYF_4$ and Er^{3+} in both $LiYF_4$ and YPO_4 correlation crystal-field interactions were also taken into account since it helped to improve the quality of the fit. For other cases the inclusion of correlation crystal-field parameters did not give a significant improvement and no values for the correlation crystal-field parameters are included in Table I.

As far as we know, the crystal-field levels of the $^2F_{5/2}$ and $^2F_{7/2}$ states of Ce^{3+} in $LiYF_4$ are not reported in the literature. Using the high-resolution $4f^{n-1}5d \to 4f^n$ emission spectrum (see the next section), five of the seven crystal-field levels could be determined (0, 216, {547}, 2221, 2316, 2430, and {3160} cm^{-1}, respectively; the predicted energies of the two unobserved levels are indicated in curly braces) and were used to fit new parameter values for the calculation of the ground-state levels. In the fit of the excited configuration parameters, the value of $\zeta(dd)$ was kept fixed at the free-ion value of 1082 and the crystal-field splitting of the d levels was taken from the excitation spectrum reported by Reid *et al.*[19]

The parameter values for the calculation of the excited $4f^{n-1}5d$ configurations are listed in Table II. The f-d Coulomb interaction parameters $F^k(fd)$ and $G^j(fd)$ are the values reported by Cowan[10] reduced to 75% for Pr^{3+} and Nd^{3+} and to 67% for Er^{3+} and Tm^{3+} (Refs. 2 and 3). The spin-orbit coupling represented by $\zeta(dd)$ and the crystal-field parameters $B_q^k(dd)$ for the $LiYF_4$ host lattice were obtained from the fit performed for Ce^{3+} by van Pieterson.[2] For the YPO_4 host lattice the ground-state levels of Ce^{3+} reported for $LuPO_4$ (Ref. 20) and the $5d$ excited-state energies reported for YPO_4 (Ref. 2) were used to obtain an "exact" fit, since the number of energy levels is equal to the number of parameters varied. The $4f$ parameters found are similar to those reported for $LuPO_4$. The $5d$ parameter values are similar to the values obtained by van Pieterson, except $\zeta(dd)$, which was kept fixed at the free-ion value of 1149 cm^{-1}, whereas we obtained a $\zeta(dd)$ of 1188 cm^{-1}.

The crystal-field parameter values for Ce^{3+} in $LiYF_4$, obtained by fitting the experimentally observed energy levels (see above), were systematically reduced across the lanthanide series following the work of van Pieterson *et al.*,[21] to

TABLE I. Parameter values (in cm^{-1}) used for the $4f^n$ energy-level calculation of Ce^{3+}, Pr^{3+}, Nd^{3+}, Er^{3+}, and Tm^{3+} in LiYF$_4$ and YPO$_4$. Parameters that were not varied are listed in brackets.

	Ce^{3+} LiYF$_4$	Pr^{3+} LiYF$_4$	YPO$_4$	Nd^{3+} LiYF$_4$	YPO$_4$	Er^{3+} LiYF$_4$	YPO$_4$	Tm^{3+} LiYF$_4$
E_{avg}	1517	10204	9999	24413	24105	35806	35569	18022
$F^2(ff)$		69025	67991	72667	71872	97449	96567	102215
$F^4(ff)$		50580	50031	52737	51793	68539	68144	72060
$F^6(ff)$		33326	32961	35817	35591	56051	53393	51366
$\alpha(ff)$		[23.00]	21.30	21.49	19.87	18.27	19.97	18.20
$\beta(ff)$		−649	−683	−585	−606	[−580]	[−632]	−686
$\gamma(ff)$		[1371]	[1371]	1424	1445	[1416]	[1800]	[1820]
$T^2(ff)$				331	[298]	[486]	[400]	[400]^a
$T^3(ff)$				43	[35]	[43]	[43]	[43]^a
$T^4(ff)$				84	[59]	[81]	[73]	[73]^a
$T^6(ff)$				−324	[−285]	[−327]	[−271]	[−271]^a
$T^7(ff)$				387	[332]	[300]	[308]	[308]^a
$T^8(ff)$				322	[305]	[346]	[299]	[299]^a
$\zeta(ff)$	628	750.1	742.1	870.1	876.3	2374	2364	2633
$B_0^2(ff)$	316	541	73	400	329	306	210	354
$B_0^4(ff)$	[−1150]	−1093	324	−1122	273	−581	81	−631
$B_4^4(ff)$	−1264	−1327	−856	−1272	−758	−917	−670	−851
$B_0^6(ff)$	[−89]	−45	−1278	−28	−1226	−6	−704	−171
$B_4^6(ff)$	−821	−1165	7	−1093	−89	−637	−61	−627
$M_0(ff)^b$		[2.00]	0.99	0.66	2.11	3.91	5.48	4.67
$P_2(ff)^c$		215	220	162	284	579	802	720
$D^2(ff)$		−15.9		4.9		5.3		
$D^4(ff)$		8.8		10.1		4.0	−1.02	

^{a}Only for the excited $4f^{11}5d$ configuration.
^{b}M$_2$ and M$_4$ parameter values were included with the ratios M_2/M_0=0.56 and M_4/M_0=0.31.
^{c}P$_4$ and P$_6$ parameter values were included with the ratios P_4/P_2=0.5 and P_6/P_2=0.1.

correct for changes in the crystal field caused by the lanthanide contraction.^{3} In addition, the spin-orbit parameter values were systematically increased across the lanthanide series. In contrast, all the excited configuration crystal-field and spin-orbit parameter values were fit for Ce^{3+} in YPO$_4$ (see previous paragraph). The parameter values for YPO$_4$ were systematically modified across the lanthanide series using the same scaling factors as for LiYF$_4$.

The $\Delta_E(fd)$ values were adjusted to set the calculated energy of the zero-phonon line for the lowest $4f^{n-1}5d \rightarrow 4f^n$

TABLE II. Parameter values (in cm^{-1}) used for the $4f^{n-1}5d$ energy-level calculation of Ce^{3+}, Pr^{3+}, Nd^{3+}, Er^{3+}, and Tm^{3+} in LiYF$_4$ and YPO$_4$.

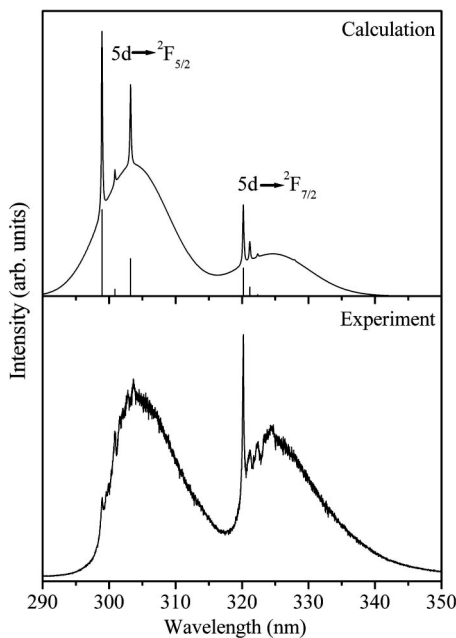|	Ce^{3+} LiYF$_4$	Pr^{3+} LiYF$_4$	YPO$_4$	Nd^{3+} LiYF$_4$	YPO$_4$	Er^{3+} LiYF$_4$	YPO$_4$	Tm^{3+} LiYF$_4$
$\Delta_E(fd)$	43773	50966	47021	56684	52772	89762	86822	94218
$F^2(fd)$		22703	22703	22543	22543	19724	19724	19639
$F^4(fd)$		11321	11321	11188	11188	9358	9358	9275
$F^6(fd)$		9677	9677	9608	9608	8038	8038	7991
$G^3(fd)$		8370	8370	8284	8284	6848	6848	6789
$G^5(fd)$		6518	6518	6442	6442	5292	5292	5240
$\zeta(dd)$	[1082]	1149	1188	1216	1257	1768	1821	1839
$B_0^2(dd)$	4673	4626	4763	4598	4734	4290	4417	4252
$B_0^4(dd)$	−18649	−18463	2221	−18351	2208	−17120	2060	−16971
$B_4^4(dd)$	−23871	−23632	−22568	−23489	−22431	−21914	−20927	−21723

FIG. 1. Calculated and measured emission spectra of LiYF$_4$:Ce^{3+} 1% with excitation at 157 nm at 10 K. In the upper spectrum, the bars give information on the positions and intensities calculated for the zero-phonon lines, while the spectrum is obtained by superimposing a Gaussian band (offset 600 cm^{-1}, width 1000 cm^{-1}) on the zero-phonon lines which have been given a width of 20 cm^{-1}. The same procedure is used in Figs. 2–9.

emission equal to the experimentally observed zero-phonon line in the emission spectrum.

B. Emission spectra

1. Cerium

The high-resolution $5d \to 4f$ emission spectrum of LiYF$_4$:Ce^{3+} 1% with 193 nm excitation at 10 K is shown in Fig. 1. The spectrum shows two broad emission bands with the highest-energy zero-phonon lines at 298.94 and 320.20 nm, which corresponds to emission from the $5d$ level to the lowest-energy crystal-field components of the $^2F_{5/2}$ and $^2F_{7/2}$ states of cerium. The energy difference observed between the $^2F_{5/2}$ and $^2F_{7/2}$ levels is 2221 cm^{-1}. Figure 1 also shows the simulated $5d \to 4f$ emission spectrum of LiYF$_4$:Ce^{3+} based on the $5d$ parameters reported by van Pieterson *et al.*[2] and the $4f$ parameters obtained from a fit to the positions of the $^2F_{5/2}$ and $^2F_{7/2}$ crystal-field components in the measured emission spectrum. The parameter values for the calculation are listed in Tables I and II. Besides the zero-phonon lines the spectrum also shows some weak vibronic lines. The low intensity of the highest-energy zero-phonon line in the experimental spectrum is due to resonant reabsorption of this emission.

2. Praseodymium

Figure 2 shows the calculated and the experimentally observed emission spectrum of LiYF$_4$:Pr^{3+} 1% with excitation at 157 nm. The assignment of transitions is indicated in the
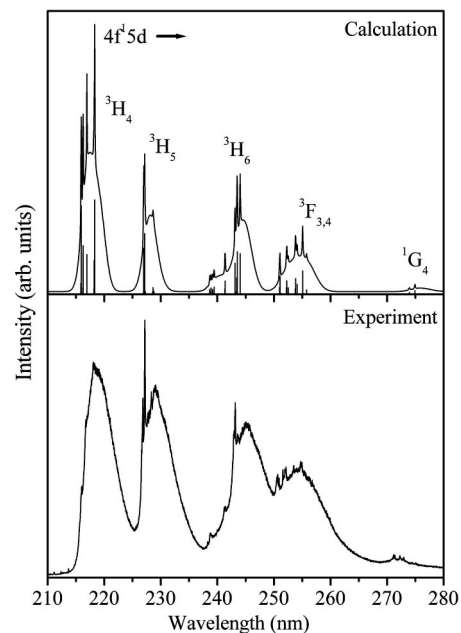

FIG. 2. Calculated and measured emission spectra of LiYF$_4$:Pr^{3+} 0.1% with excitation at 157 nm at 10 K. See also Fig. 1.

figure. Fine structure is observed for all emission bands except for the highest-energy emission. No clear vibronic progression can be observed in the emission spectrum. The intensity ratios of the emission lines are in excellent agreement with the ratios shown in the simulated spectrum. There is a very good agreement for the calculated and observed intensities of the fd emission bands to the different $4f^2$ multiplets: for all transitions the band calculated as intense bands are strong, weak bands are weak and the relative integrated intensities agree within 20% between experiment and calculation. For the relative intensities of individual zero-phonon lines within a certain multiplet the variations are somewhat larger. For example, for the $fd \to {}^3H_6$ transition not all calculated zero-phonon lines are observed. The experimentally observed energies of the fd emission bands coincide with the calculated energies, except for the $fd \to {}^1G_4$ emission band. The calculated position of the emission to the $^1G_4$ levels situated at 272 nm, however, is too low. It is known for certain lanthanide ions like Pr^{3+} that the one-electron crystal-field parametrization gives an accurate description of the crystal-field levels for most multiplets, but not for all of them.[22] Therefore we also included the δ-function correlation crystal-field parameters D_q^k for $k=2$ and 4 using the δ functions as reported by Lo and Reid.[24] The inclusion of two-electron correlation crystal-field interactions was shown to improve the calculated splitting of the anomalously behaving multiplets,[23] but even with inclusion of correlation crystal-field interaction parameters, the calculation model predicts the position of the $^1G_4$ at a somewhat different energy. The parameter values used for the calculation are summarized in Tables I and II.

Figure 3 shows the calculated and experimentally observed emission spectrum of YPO$_4$:Pr^{3+} 1% with excitation at 157 nm. Besides sharp zero-phonon lines this spectrum
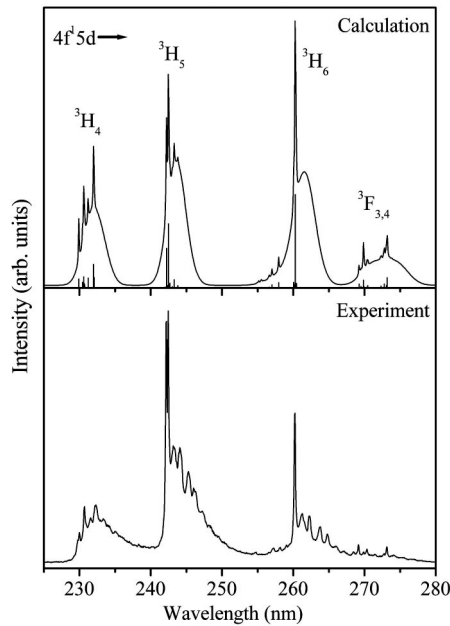
FIG. 3. Calculated and measured emission spectra of YPO$_4$:Pr^{3+} 1% with excitation at 157 nm at 10 K. See also Fig. 1.

also displays a clear vibronic structure on the emission bands for the transitions to the $^3H_4$, $^3H_5$, and $^3H_6$ multiplets. The parameter values used for the calculation are summarized in Tables I and II. The intensities of the emission bands and the relative intensities of the zero-phonon lines of the experiment are closely reproduced in the calculated spectrum. Also the positions of the zero-phonon lines are in good agreement. Clearly, the model and the parameter values for the $4f^{n-1}5d$ states and the $4f^n$ states for Pr^{3+} in YPO$_4$ give a good description of the actual states involved.

The main difference between the experimental and calculated spectrum is in the vibronic structure. In the model, a vibronic Gaussian band is superimposed on the zero-phonon line. For the $4f^{n-1}5d \rightarrow 4f^n$ emission spectra for the lanthanide ions in LiYF$_4$ a broad vibronic band gives a reasonably good description since vibronic features are not clearly observed. However, in the case of YPO$_4$ the Huang-Rhys factor is smaller for the $4f^{n-1}5d \rightarrow 4f^n$ transitions which results in a higher relative intensity of the zero-phonon lines and the observation of sharp vibronic lines corresponding to coupling with well-defined vibrational modes. From the analysis of the vibronic lines in Fig. 3 vibrational modes of 148 cm^{-1} and 370 cm^{-1} can be observed. A further analysis of the vibronic structure of the $4f^{n-1}5d \rightarrow 4f^n$ emission bands in YPO$_4$ is an interesting topic for further studies.

3. Neodymium

The spectra depicted in Fig. 4 and 5 show the calculated and experimentally observed $4f^25d \rightarrow 4f^3$ emission spectrum of LiYF$_4$:Nd^{3+} and YPO$_4$:Nd^{3+}, respectively, with excitation at 157 nm at 10 K. The emissions to the $^4I_{9/2}$, $^4I_{11/2}$, and $^4I_{13/2}$ levels are shown and indicated in the figures. For both LiYF$_4$:Nd^{3+} and YPO$_4$:Nd^{3+} the positions and intensities of the zero-phonon lines in the simulated spectra are in good
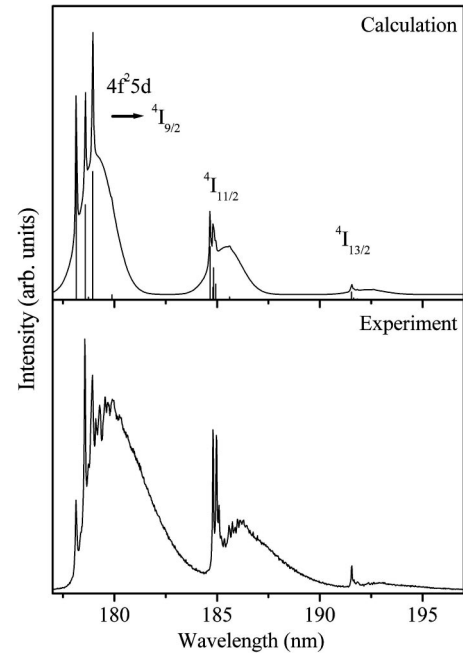

FIG. 4. Calculated and measured emission spectra of LiYF$_4$:Nd^{3+} 1% with excitation at 157 nm at 10 K. See also Fig. 1.

agreement with the experimentally obtained spectra. The calculated and observed relative intensities of the three emission bands and also the relative intensities of individual zero-phonon lines do not vary by more than 50%. In view of the large variations of the relative intensities, we consider this as a good agreement. The intensity of the highest-energy zero-phonon line of the emission to the $^4I_{9/2}$ levels for both LiYF$_4$:Nd^{3+} and YPO$_4$:Nd^{3+} is lower in the experimental spectrum due to reabsorption. In the emission spectrum of LiYF$_4$:Nd^{3+}, a vibronic structure is visible, albeit weak. For
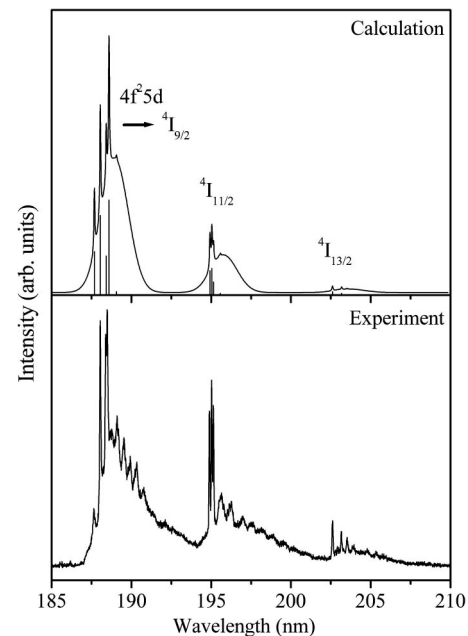

FIG. 5. Calculated and measured emission spectra of YPO$_4$:Nd^{3+} 1% with excitation at 157 nm at 10 K. See also Fig. 1.

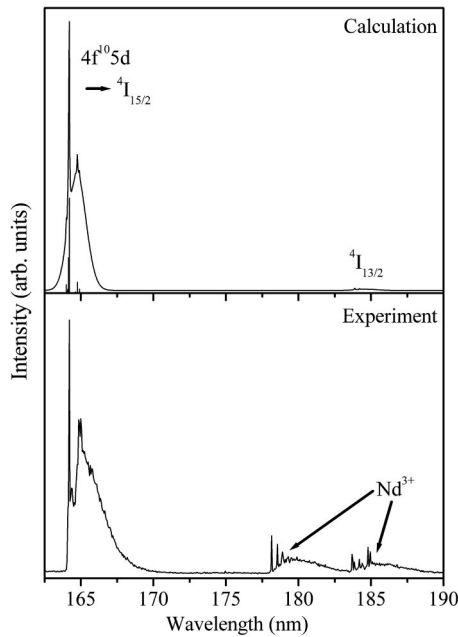FIG. 6. Calculated and measured emission spectra of $LiYF_4$:Er^{3+} 1% with excitation at 157 nm at 10 K. See also Fig. 1.

FIG. 7. Calculated and measured emission spectra of YPO_4:Er^{3+} 1% with excitation at 157 nm at 10 K. See also Fig. 1.

YPO_4:Nd^{3+}, a clear vibronic progression is observed just as for YPO_4:Pr^{3+}. Due to the presence of many zero-phonon lines, it is not possible to assign energies to vibrations unambiguously. The parameter values used for the calculations are summarized in Tables I and II.

4. Erbium

In Fig. 6, the calculated and experimentally observed emission spectrum of $LiYF_4$:Er^{3+} with 157 nm excitation at 10 K are shown. At this excitation wavelength, only the high-spin $4f^{10}5d$ state is populated [the onset of the low-spin excitation is at 155 nm (Ref. 3)] and as a result only spin-forbidden emission is observed. The emission from the high-spin $4f^{10}5d$ state to the $^4I_{15/2}$ ground state is very intense compared to the emission to the $^4I_{13/2}$ level. The much higher relative intensity of the higher-energy emission band is reproduced in the calculated emission spectrum. In fact, the calculated relative intensity of the emission band to the $^4I_{13/2}$ level is even weaker than in the experiment. This may be (partly) due to the fact that the emission spectra could not be corrected for the wavelength dependence of the instrumental response. Note that the observation of the weak $4f^{10}5d \rightarrow 4f^{11}(^4I_{13/2})$ emission band is hampered by the presence of emission bands around 180 nm and 185 nm due to a contamination with Nd^{3+}. The fact that these emissions show up as relatively strong bands is due to the fact that at 157 nm the Er^{3+} ion is excited in a spin-forbidden transition while the Nd^{3+} ion has a strong spin-allowed absorption band. The small relative intensity of the emission band corresponding to the $4f^{10}5d \rightarrow 4f^{11}(^4I_{13/2})$ transition can be understood on the basis of J selection rules. Transitions with $\Delta J > 1$ are forbidden and appear only by means of J mixing of the states. The lowest calculated high-spin $4f^{10}5d$ state has 89% contributions of $J=17/2$ states. In accordance with the ΔJ
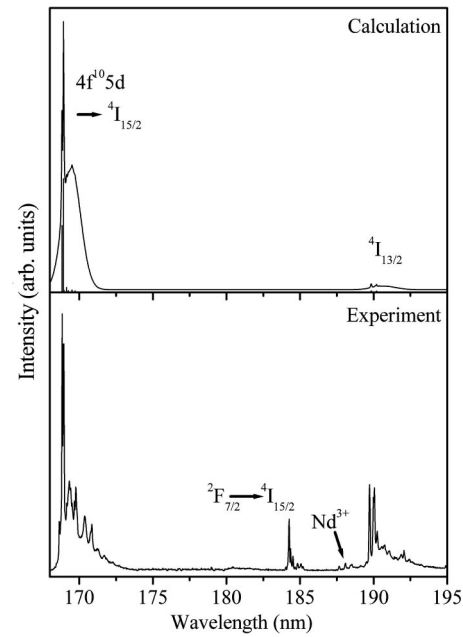
selection rule, the highest emission intensity is expected for the emission to the $^4I_{15/2}$ ground state, which is observed in both the simulated and experimental emission spectra.

In Fig. 7, the calculated and experimentally observed emission spectra of YPO_4 doped with Er^{3+} with 157 nm excitation at 10 K is shown. At this excitation wavelength, the low-spin $4f^{10}5d$ state is populated,[3] and after relaxation to the high-spin state, spin-forbidden emission is observed. Just as in $LiYF_4$, the emission from the high-spin $4f^{10}5d$ state to the $^4I_{15/2}$ ground state is very intense compared to the emission to the $^4I_{13/2}$ level. The measured intensity ratio between the emissions to the $^4I_{15/2}$ and $^4I_{13/2}$ levels differs from the calculated intensity ratio. The relative intensity of the higher-energy band is expected to increase if the spectrum could be corrected for the wavelength dependence of the instrumental response—resulting in a better agreement with the calculated spectrum. The parameter values used for the calculation are summarized in Tables I and II. The emission band at 170 nm shows a clear vibronic progression. The weak emissions at 188 nm are due to contamination of the sample with neodymium. The sharp emission lines at 184 nm are due to the intraconfigurational $4f^n$ $^2F_{7/2} \rightarrow {}^4I_{15/2}$ transition of erbium. For YPO_4:Er^{3+}, the influence of the ΔJ selection rule is also observed. The lowest calculated high-spin $4f^{10}5d$ state has 81% contributions of $J=17/2$ states. According to the ΔJ selection rule, the highest emission intensity is expected (and calculated) for the emission to the $^4I_{15/2}$ ground state, which is indeed observed in the spectrum.

5. Thulium

Figure 8 shows the calculated and experimentally observed emission spectrum of $LiYF_4$ doped with Tm^{3+}. Using excitation at 157 nm, emission is observed from both the high-spin and low-spin $4f^{11}5d$ states. The corresponding
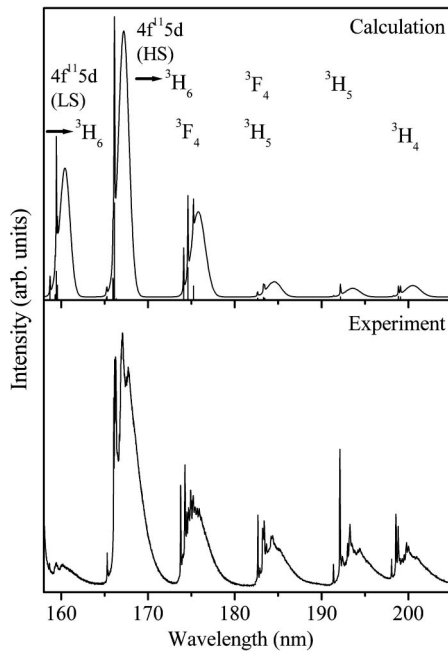
FIG. 8. Calculated and measured emission spectra of LiYF$_4$:Tm^{3+} 1% with excitation at 157 nm at 10 K. The spin-allowed and spin-forbidden emission spectra were calculated separately and their relative intensity was set to match the experimentally observed spectrum. See also Fig. 1.

simulated emission spectra were calculated separately and plotted with a ratio of the high-spin to low-spin emission intensity chosen to match the experimentally observed spectrum. The parameter values used for the calculations are summarized in Tables I and II. The calculated and measured intensities are in good agreement, except for the spin-allowed emission to the $^3H_6$ levels at 160 nm, which is weaker in the experimental spectrum. This is due to the low sensitivity of the photomultiplier tube at this wavelength. The steep increase on the left-hand side of the experimental spectrum is a due to scattered 157-nm radiation of the laser.

Using gated detection, it was possible to record an emission spectrum for LiYF$_4$:Tm^{3+} showing only the spin-forbidden emissions. The spin-allowed *fd* emission for Tm^{3+} in LiYF$_4$ has a 16-ns lifetime,[21] and by applying gated detection with a delay of 1 μs and a gate of 5 μs, only the longer lived spin-forbidden emission (τ=5.4 μs) is detected. The resulting emission spectrum is depicted in Fig. 9 together with the calculated spin-forbidden emission spectrum. The intensity ratios of the zero-phonon lines in the emission spectra show a good agreement with the calculated intensities.

C. Luminescence lifetime measurements

The lifetime of the spin-forbidden $4f^{n-1}5d \rightarrow 4f^n$ emission was measured for Er^{3+} in LiYF$_4$ and YPO$_4$ and for Tm^{3+} in LiYF$_4$. In Fig. 10, a typical example of a luminescence decay curve is shown. The luminescence decay is well described by a single exponential with a lifetime of the order of μs. The experimentally observed lifetimes are included in Table III. The presently reported lifetimes are somewhat different from
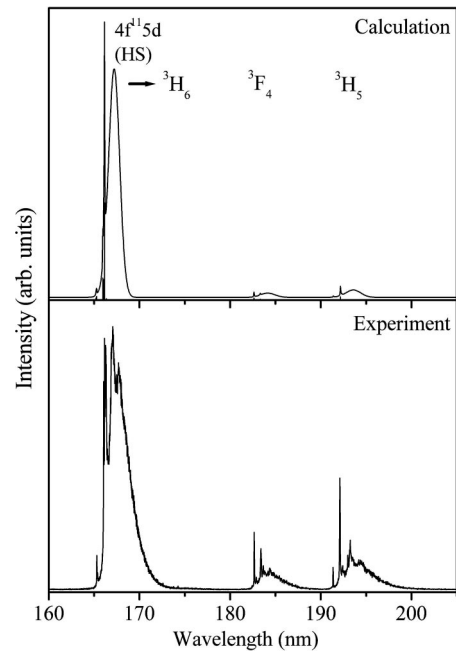
values published previously by us and other groups.[21,25] The reason is that in previous work the lifetimes were obtained from luminescence decay curves measured using a synchrotron. The repetition rate (typically MHz) of synchrotron radiation is determined by the round-trip time of bunches in the ring and is too high to accurately determine lifetimes that are μs or longer. For MHz repetition rates the decrease in signal between two pulses is limited, and the determination of the lifetime from the fit to a single exponential is rather inaccurate. With the presently used VUV laser with a much lower repetition rate (typically 100 Hz), the luminescence lifetimes can be accurately determined in the μs−ms range. We therefore believe that the values for the lifetimes in Table III are more reliable than previously reported values.
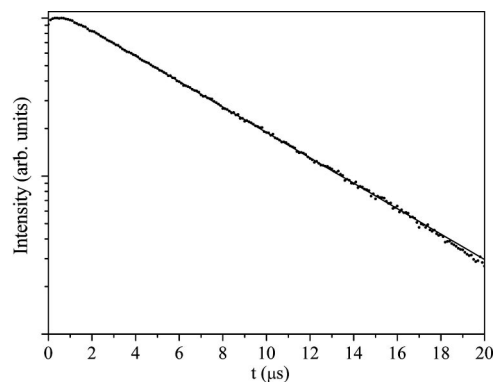

FIG. 9. Calculated and measured spin-forbidden emission spectra of LiYF$_4$:Tm^{3+} with excitation at 157 nm at 10 K using gated detection (delay 1 μs, gate 5 μs). See also Fig. 1.

FIG. 10. Luminescence decay curve of the spin-forbidden $4f^{10}5d \rightarrow 4f^{11}$ emission at 168 nm of LiYF$_4$:Tm^{3+} with excitation at 157 nm at 10 K. The dots give the measured time dependence of the luminescence intensity and the drawn line gives the best fit to a single-exponential decay with τ=5.4 μs. Note that the vertical axis is a logarithmic scale.

TABLE III. Radial integrals $\langle 5d|r|4f \rangle$ and calculated and experimentally observed lifetimes for the spin-forbidden emissions of Er^{3+} and Tm^{3+} in $LiYF_4$ and YPO_4.

	Wavelength (nm)	τ_{expt} (μs)	τ_{calc} (μs)	$\langle 5d|r|4f \rangle^a$ (Å)
$LiYF_4:Er^{3+}$	167	2.4	4.2	0.304
$YPO_4:Er^{3+}$	170	1.0	3.4	0.304
$LiYF_4:Tm^{3+}$	168	5.4	13.1	0.291

[a]Reference 10.

Since $4f^{n-1}5d \to 4f^n$ transitions are parity-allowed electric-dipole transitions, it is relatively simple to calculate the radiative transition probability. Using Eq. (8) and the parameter values from Tables I and II, the radiative decay rates were determined using radial integrals $\langle 5d|r|4f \rangle$ tabulated in Table III. The general trend in the decay times is well reproduced by the calculation and also the order of magnitude is correct. However, the experimentally obtained decay times are a factor of 3 lower than the calculated values. It is, at this time, not clear what causes the difference. Most probably it is related to the radial integrals $\langle 5d|r|4f \rangle$. The transition probabilities are very sensitive to small changes in this integral. The radial integrals are calculated for the free ion using Cowan's program.[10] In the crystal, the radial integral will change due to covalency effects, and this may explain the difference between calculated and experimentally observed luminescence decay times. For $YPO_4:Er^{3+}$, the shortening of the lifetime observed may also be partly due to fast nonradiative decay from the lowest high-spin $4f^{10}5d$ level to the $^2F(2)_{7/2}$ level of erbium. The energy difference in the order of 5000 cm^{-1} is approximately 5 times the maximum phonon energy in YPO_4 and multiphonon relaxation from the lowest high-spin $4f^{10}5d$ level to the $^2F(2)_{7/2}$ level is expected.[26]

V. CONCLUSIONS

High-resolution $4f^{n-1}5d \to 4f^n$ emission spectra of Pr^{3+} Nd^{3+} Er^{3+}, and Tm^{3+} in $LiYF_4$ and YPO_4 have been measured and compared with the calculated emission spectra using a recently developed model for $4f^{n-1}5d$ states. The emission spectra show a well-resolved fine structure with sharp zero-phonon lines and, especially in the YPO_4 host lattice, vibronic lines. In general, good agreement between the calculations and experiment was found for the relative intensities and energies of zero-phonon lines corresponding to $4f^{n-1}5d \to 4f^n$ transitions to the lower-energy $4f^n$ states, demonstrating the validity of the model used. Luminescence lifetimes for the spin-forbidden $4f^{n-1}5d \to 4f^n$ emissions were calculated and found to be longer than the experimentally observed lifetimes.

*Electronic address: p.s.peijzel@phys.uu.nl

[1] P. S. Peijzel, R. T. Wegh, A. Meijerink, J. Hölsä, and R. J. Lamminmäki, Opt. Commun. **204**, 195 (2002).

[2] L. van Pieterson et al., Phys. Rev. B **65**, 045113 (2002).

[3] L. van Pieterson, M. F. Reid, G. W. Burdick, and A. Meijerink, Phys. Rev. B **65**, 045114 (2002).

[4] Y. Chen et al., Phys. Status Solidi B **240**, R1 (2003).

[5] P. S. Peijzel, A. Meijerink, R. T. Wegh, M. F. Reid, and G. W. Burdick, J. Solid State Chem. (to be published).

[6] C. Görller-Walrand and K. Binnemans, in *Handbook on the Physics and Chemistry of Rare Earths*, edited by J. K. A. Gschneider and L. Eyring (Elsevier, Amsterdam, 1996), Vol. 23, pp. 121–283.

[7] B. Henderson and G. F. Imbush, *Optical Spectroscopy of Inorganic Solids* (Clarendon Press, Oxford, 1989).

[8] O. Guillot-Noel, B. Bellamy, B. Viana, and D. Gourier, Phys. Rev. B **60**, 1668 (1999).

[9] G. F. Imbush and R. Copelman, in *Laser Spectroscopy of Solids*, edited by W. M. Yen and P. M. Selzer (Springer, New York, 1981).

[10] R. D. Cowan, *The Theory of Atomic Structure and Spectra* (University of California, Berkeley, 1981).

[11] B. G. Wybourne, *Spectroscopic Properties of Rare Earths* (Interscience Publishers, New York, 1965).

[12] L. A. Boatner, *Synthesis, Structure, and Properties of Monazite, Pretulite, and Xenotime in Phosphates: Geochemical, Geobiological, and Materials Importance*, edited by M. J. Kohn, J. Rakovan, and J. M. Hughes, Vol. 48 of *Reviews in Mineralogy and Geochemistry* (Mineralogical Society of America, 2002).

[13] G. W. Burdick and F. S. Richardson, Chem. Phys. **228**, 81 (1998).

[14] T. Hayhurst, G. Shalimoff, N. Edelstein, L. A. Boatner, and M. M. Abraham, J. Chem. Phys. **76**, 3960 (1982).

[15] A. A. S. da Gama, G. F. de Sá, P. Porcher, and P. Caro, J. Chem. Phys. **75**, 2583 (1981).

[16] M. A. Couto dos Santos, E. Antic-Fidancev, J. Y. Gesland, J. C. Krupa, M. Lemaître-Blaise, and P. Porcher, J. Alloys Compd. **275–277**, 435 (1998).

[17] T. Hayhurst, G. Shalimoff, N. Edelstein, L. A. Boatner, and M. M. Abraham, J. Chem. Phys. **74**, 5449 (1981).

[18] H. P. Jenssen, A. Linz, R. P. Leavitt, C. A. Morrison, and D. E. Wortman, Phys. Rev. B **11**, 92 (1975).

[19] M. F. Reid, L. van Pieterson, R. T. Wegh, and A. Meijerink, Phys. Rev. B **62**, 14 744 (2000).

[20] G. M. Williams, P. C. Becker, J. G. Conway, N. Edelstein, L. A. Boatner, and M. M. Abraham, Phys. Rev. B **40**, 4132 (1989).

[21] L. van Pieterson, R. T. Wegh, A. Meijerink, and M. F. Reid, J. Chem. Phys. **115**, 9382 (2001).

[22] Y. Y. Yeung and D. J. Newman, J. Chem. Phys. **86**, 6717 (1987).

[23] G. W. Burdick and F. S. Richardson, Chem. Phys. **228**, 81 (1998).

[24] T. S. Lo and M. F. Reid, J. Alloys Compd. **193**, 180 (1993).

[25] V. N. Makhov, N. M. Khaidukov, N. Y. Kirikova, M. Kirm, J. C. Krupa, T. V. Ouvarova, and G. Zimmerer, J. Lumin. **87–89**, 1005 (2000).

[26] R. T. Wegh, W. van Klinken, and A. Meijerink, Phys. Rev. B **64**, 045115 (2001).